Journal of Materials Chemistry A

ROYAL SOCIETY OF CHEMISTRY

PAPER

View Article Online
View Journal | View Issue

Cite this: J. Mater. Chem. A, 2023, 11, 13677

3D printing of self-supported solid electrolytes made of glass-derived $Li_{1.5}Al_{0.5}Ge_{1.5}P_3O_{12}$ for all-solid-state lithium-metal batteries†

A. G. Sabato, *[a] M. Nuñez Eroles,[a] S. Anelli, [ab] C. D. Sierra,[a] J. C. Gonzalez-Rosillo, [a] M. Torrell, [a] A. Pesce, [c] G. Accardo, [c] M. Casas-Cabanas, [cd] P. López-Aranguren, [c] A. Morata [a] and A. Tarancón *[ae]

Additive manufacturing (AM) techniques using advanced functional materials are attracting strong attention in the field of all solid-state lithium batteries (ASSBs) since they are considered as innovative approaches that will pave the way for cheaper, safer, and customizable batteries with exceptional volumetric energy density. In the present work, stereolithography (SLA) is presented as a suitable technique to produce complex-shaped $Li_{1.5}Al_{0.5}Ge_{1.5}P_3O_{12}$ (LAGP) full-ceramic electrolytes from glass feedstock. Printed electrolytes showed an ionic conductivity in good agreement with LAGP fabricated by conventional techniques ($\sigma = 6.42 \times 10^{-5}$ S cm^{-2}). Moreover, 3D printed LAGP corrugated membranes with interfacial area increased by 15% were fabricated showing an equivalent reduction of the area specific resistance. Symmetrical cells with lithium metal electrodes were used to study the stripping and plating behaviour of LAGP printed electrolytes coated with a germanium protective interlayer deposited *via* thermal evaporation. The symmetric cells showed a stable cycling performance over 250 hours demonstrating the stability of the designed cells. The innovative approach reported here represents the first step for the next generation of ASSBs based on LAGP, offering new degrees of freedom for the manufacturing of full ceramic electrolytes with a complex shape.

Received 8th March 2023
Accepted 13th May 2023

DOI: 10.1039/d3ta01435e

rsc.li/materials-a

1 Introduction

Lithium-ion batteries have been widely studied and developed in the last few decades thanks to their high energy and power density.[1,2] Nowadays, this technology is mainly based on the use of organic liquid electrolytes due to their superior ionic conductivity. However, typical liquid electrolytes are characterized by a reduced lifetime, safety issues (*i.e.* high flammability), toxicity, and high manufacturing costs.[3,4] For these reasons, many efforts have been dedicated in recent years to the development of solid-state electrolytes (SSEs) for their ultimate use in all-solid-state batteries (ASSBs). The development of SSEs compatible with existing high-voltage positive materials and, furthermore, metallic lithium anodes, is currently the main research challenge in the field. The materials typically considered as SSEs can be of polymeric or ceramic nature such as PEO and PVDF-HFP or $Li_{1+x}Al_xTi_{2-x}(PO_4)_3$ (LATP), $Li_{1+x}Al_xGe_{2-x}(PO_4)_3$ (LAGP) and $Li_7La_3Zr_2O_{12}$ (LLZO), respectively.[5,6] Complementarily, many studies have been focused on the combination of both approaches developing polymer/ceramic composite solutions.[7,8]

Together with the development of new and enhanced materials, many efforts have also been devoted to the processing of ASSBs. This is due to the intrinsic limitations in performance of state-of-the-art 2D planar structures. For this reason, in the last few years, additive manufacturing fabrication techniques such as 3D printing received increasing attention for these particular applications, with the aim to achieve higher energy and power densities.[9–12] 3D-printing is an emerging disruptive manufacturing technique, especially for ceramic materials, which can build an object layer by layer starting from a computer-aided design (CAD) that allows the production of complex shapes with a reduced amount of waste materials. Typical printing techniques used in the field of the energy devices are inkjet, robocasting, fused deposition modelling and stereolithography (SLA).[13–15]

Robocasting has been one of the most employed tools for 3D-printing of energy devices like fuel cells, supercapacitors, or

[a]Catalonia Institute for Energy Research (IREC), Department of Advanced Materials for Energy, Jardins de les Dones de Negre 1, 2nd Floor, 08930 Sant Adria de Besos, Barcelona, Spain. E-mail: gsabato@irec.cat; atarancon@irec.cat
[b]Politecnico di Torino, Department of Applied Science and Technology (DISAT), Corso Duca degli Abruzzi 24, 10129, Turin, Italy
[c]Center for Cooperative Research on Alternative Energies (CIC energiGUNE), Basque Research and Technology Alliance (BRTA), Alava Technology Park, Albert Einstein 48, 01510 Vitoria-Gasteiz, Spain
[d]Ikerbasque Basque Foundation for Science, 48013 Bilbao, Spain
[e]ICREA, Passeig Lluís Companys 23, 08010 Barcelona, Spain

† Electronic supplementary information (ESI) available. See DOI: https://doi.org/10.1039/d3ta01435e

batteries.[16] However, it is characterized by a poor resolution (in the order of 100 s of μm), low-quality surface finishing, and strong limitations to fabricate complex shapes such as those involving suspended structures.[17] Alternatively, 3D printing techniques based on light processing can overcome these limitations presenting resolution in the order of 10 s of μm, excellent surface finishing and remarkable shape freedom. In particular, SLA is based on layer-by-layer curing of photosensitive resins loaded with ceramic particles by exposure to a focused light source, often a laser in the ultraviolet range. Photo-curable slurries for ceramic SLA printing are usually characterized by high solid concentrations (40–60 vol%) reducing the risk of defect formation during drying and debinding/sintering steps,[18] making the technique especially suitable for the fabrication of dense parts.[19] In this regard, SLA has successfully been employed in the fabrication of dense electrolytes with complex shapes for energy conversion fields like solid oxide cells.[15,20–22] In particular, 8 mol% yttria-stabilized zirconia (8YSZ) has been successfully developed for SLA manufacturing by the authors. It represents a state-of-the-art electrolyte for solid oxide cell applications,[21] with corrugated shapes, which led to an increase in the performance of the cell up to 57%.

In the particular case of ASSBs, 3D printing represents a remarkable advantage aiming to increase the energy density of batteries by design for portable applications that require a high degree of customization such as off-grid applications, IoT or wearable electronics.[23] Despite the potential of this manufacturing technology, 3D printing of batteries remains mostly unexplored. A majority of the existing studies are focused on individual electrode materials printed by inkjet or robocasting.[24–28] Among these, one can highlight the pioneering work by Sun *et al.*[29] who successfully printed LTO and LFP electrodes by robocasting for building up an interdigitated micro-battery, using a liquid ionic conductor as electrolyte. Considering NASICON-type ceramic electrolytes, Zekoll *et al.*[30] dealt with 3D architectures of LAGP which acted as a hosting structure for a polymeric Li conductor. In this case SLA was used to produce complex sacrificial scaffolds to be impregnated by LAGP. Subsequently the sacrificial material was burnt and the LAGP was sintered allowing the production of complex shapes suitable to be infiltrated with the polymer. In general, most of the reports on 3D printing of batteries involve the use of liquid or polymeric electrolytes,[31–33] limiting the intrinsic benefits of using ceramic electrolytes and developing full-ceramic batteries. An important exception is the work by McOwen *et al.*[34] where the authors reported the 3D-printing of garnet-type (LLZO) electrolytes (on LLZO membranes) suitable for electrode infiltration, therefore increasing the interfacial electrolyte/electrode area and, consequently, the specific performance per unit area.

In this work, we present for the first time, a proof of concept of the application of SLA for printing self-supported ceramic electrolytes for Li-ion batteries. Whilst the procedure can be universally applied to a wide class of ceramic ionic conductors, the proof of concept is carried out using a relevant material in the field such as the glass-derived LAGP NASICON-type electrolyte. Electrolytes of this family present high ionic conductivity (10^{-4}–10^{-3} S cm^{-1}) and are ideal candidates for ceramic electrolytes thanks to their high chemical, dimensional and thermal stability.[35,36] Moreover, they show lower sintering temperatures in comparison with other ceramic materials.[37–39] The ionic conductivity of 3D printed electrolytes is measured by using electrochemical impedance spectroscopy employing gold electrodes. Finally, a thin layer of Ge is deposited by sputtering at the interface between LAGP and Li metal to improve the cycling performance of symmetric cells.

2 Experimental

2.1 Sample fabrication and characterization

Amorphous $Li_{1.5}Al_{0.5}Ge_{1.5}P_3O_{12}$ (LAGP) was selected as the electrolyte material. Commercial powders with a $d(50) \approx 5.3$ μm and a volumetric specific surface area of $\approx 1.2\ 10^4$ cm^2 cm^{-3} (Toshima Manufacturing Co. Ltd, Japan) were used for the fabrication of pellets and 3D printed parts. The material, received in its glassy state, was first characterized in order to optimize the debinding and sinter-crystallization thermal treatment.

High temperature X-ray diffraction (HT-XRD) analyses were carried out in air, starting at room temperature (RT) up to 800 °C and returning to RT. XRD patterns were recorded at different temperatures: RT before the thermal cycle, and 550 °C, 600 °C, 700 °C, 800 °C and RT, after cooling (20 min acquisition time per temperature and 5 °C min^{-1} heating/cooling rate). The diffractometer used was a Bruker D8 Advance (USA) equipped with a heating chamber and Cu-Kα radiation (1.5418 A) as incident beam. Based on these results and the results collected by differential scanning calorimetry (DSC – described in the ESI†), the optimal sinter-crystallization temperature was identified at 750 °C. LAGP amorphous powders were pressed in the form of pellets at 1 MPa. The pressed pellets were densified at 750 °C in air for 12 h in a muffle furnace (Lenton Furnaces & Ovens, Uk).

Scanning electron microscopy (SEM, Auriga ZEISS, Germany) was carried out to assess the densification reached and the microstructure of the pellets and of the 3D printed parts after the thermal treatments.

The printed and sintered structures were morphologically characterized by SEM. In addition, XRD analyses were carried out in order to point out possible differences with the pattern recorded on the LAGP processed in the form of a pellet (not 3D printed).

2.2 3D printing and sintering of LAGP samples

In this work SLA additive manufacturing techniques were applied for the fabrication of the studied electrolytes. A desktop SLA printer (Form2, Formlabs, USA) operating in open mode, equipped with a UV laser with a wavelength of 405 nm (250 mW) and a spot size of 140 μm was used. The printing layer thickness was set to 50 μm (*z*-axis) ensuring a good resolution and the robustness of the printed pieces.

For the formulation of the paste, the ceramic powders were dispersed in a UV curable acrylate-based commercial resin (Tethon Genesis, Tethon, USA) and a black pigment (SpotA-

materials) was added to tailor the UV absorption of the resin. In this way, the formulation was tuned in order to reach a curing depth of 190 ± 5 μm. In addition, a dispersant additive (Monofax 057, Fischer Scientific) was added. The paste formulation was 65 wt% of LAGP, 34.35 wt% of UV-curable resin and 0.65 wt% of Monofax. The mixture was prepared by mixing the dispersant and the resin and then gradually adding the ceramic powders in three steps and mixing the compound for 5 min at 1000 rpm for each addition in a centrifugal mixer (ARE-250, Thinky corp. Japan). Finally, the pigment was added (0.5 wt% of the total weigh of the paste previously mixed) and mixed with a last step under the same conditions.

The design of the components to be printed by SLA, was performed by computer aided design (CAD) software. Two different structures were considered: a reference membrane and a corrugated one. The latter was designed to increase the interfacial area with the electrodes, and these structures are better described in Section 3. After the SLA process, the printed parts were cleaned by sonication in a Ceracleaner bath (3DCeram, France).

In order to optimize the debinding and sintering treatment of the 3D printed parts, a printed sample was analysed by DSC/TGA (results and details are reported in the ESI†). The debinding/sintering treatments were carried out in air in a muffle furnace, and consisted of: ramping up to 400 °C at 0.2 °C min^{-1}, dwelling for 2 h, ramping up to 750 °C at 5 °C min^{-1} and a dwelling of 12 h.

2.3 Electrochemical impedance measurements and symmetrical cell tests

Sintered pellets of LAGP were polished (up to #4000 grit, SiC paper) on both sides before sputtering with gold electrodes. Such cells were used for electrical characterization by electrochemical impedance spectroscopy (EIS). EIS was measured using a Novocontrol (NOVOCONTROL Technologies GmbH & Co. KG Alpha analyser) impedance analyser in a frequency range between 10^7 and 0.1 Hz applying 50 mV AC amplitude in potentiostatic mode. EIS was carried out with the sample placed in a furnace under controlled temperature and atmosphere conditions. 3D printed electrolytes, after the debinding and sintering treatment, were also tested by EIS, analogously to the analyses carried out on the pellets.

For the cycling of symmetric cells with Li metal, in order to avoid the detrimental reactions between LAGP and metallic Li, thin Ge interlayers of 200 nm were deposited *via* thermal evaporation (UNIVEX 250, LEYBOLD GmbH, and GE) on both sides of the sintered electrolytes. The deposition was carried out at a rate of 2 Å s^{-1}, using Ge chips (purity 99.999%, Sigma-Aldrich) placed in a tungsten crucible.

3D printed membranes with optimized germanium coatings were used for stability studies employing Li metal (Rockwood Lithium, battery grade) in both electrodes. Lithium electrodes were applied to the electrolyte with a light pressure under an Ar atmosphere. Such symmetrical cells were assembled in Swagelok units. Ionic conductivity in the Li/Ge-LAGP-Ge/Li configuration was additionally evaluated with EIS analysis recorded at RT after assembly, using a Solartron 1260A impedance analyzer (Solartron Metrology, UK) in the frequency range from 10^7 to 1 Hz by applying 20 mV AC amplitude. Stripping/plating tests were performed in a thermal controlled chamber (25 °C). Galvanostatic cycling was performed in a Maccor series 4000 battery tester (Maccor Inc., USA) applying current densities of 50 μA cm^{-2} and 100 μA cm^{-2} during 2 h for each semi-cycle. The overpotential of the cell was recorded over time.

3 Results and discussion

High temperature XRD experiments were carried out on the as-received amorphous LAGP powders from room temperature (RT) to 800 °C and back to room temperature (Fig. 1). Spectra collected at RT and 550 °C only show the presence of an amorphous phase, while crystalline peaks were detected after 600 °C (in good agreement with DSC analyses reported in Fig. S1†). $LiGe_2(PO_4)_2$ (PDF #1-080-1924) was identified as the only crystallized phase all along the temperature roundtrip. In this regard, despite the substitution of Ge by Al, LAGP XRD patterns are often identified with $LiGe_2(PO_4)_2$ (ref. [40–42]) with slightly shifted peaks (as is the case here). The absence of secondary phases in the spectra indicates that no detrimental reactions or degradations were taking place as a consequence of high temperature exposure to air.

In Fig. 2, the 3D CAD models of the printed parts are shown, together with pictures of the as-printed LAGP samples. In this work two geometries were considered: a reference membrane (Fig. 2a–c), and a corrugated one (Fig. 2d–f). In both geometries,

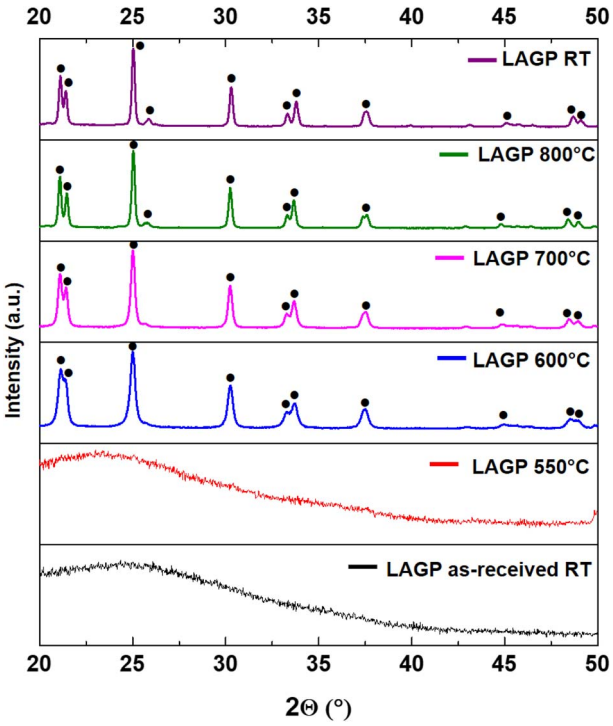

Fig. 1 HT-XRD of LAGP powders, the peaks of the crystallized phase (•) were identified with $LiGe_2(PO_4)_2$ (PDF #1-080-1924).

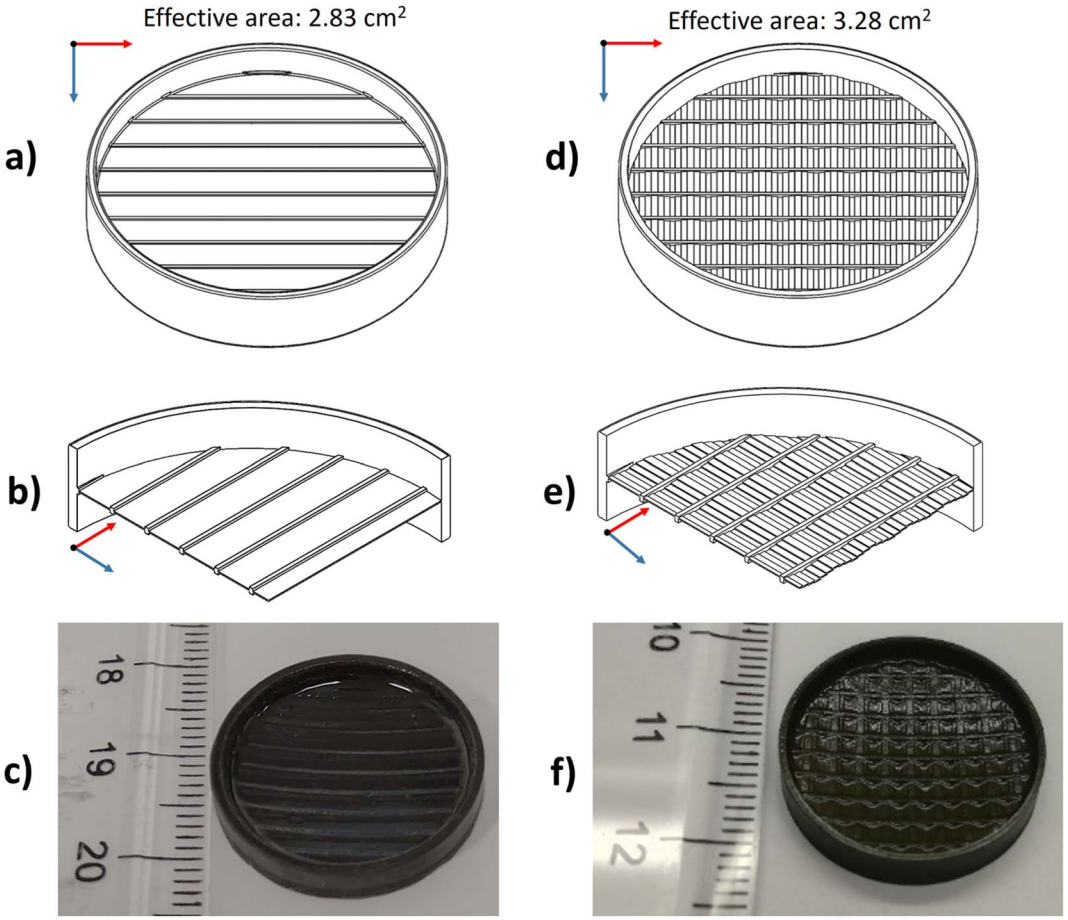

Fig. 2 3D CAD drawings, details of the cross-sections and photo of the as-printed membranes: reference (a–c) and corrugated (d–f).

some structural elements such as an external ring and ribs were incorporated to improve the mechanical integrity of the parts during the printing and post-printing processes and to limit deformations during the following sintering treatment. These elements do not contribute to the ionic conduction of the component and are identical in both designs. The two designs present the same projected area; however, when the effective area is considered, the corrugation introduces an increase of ≈15% in the case of the corrugated membrane (2.83 cm^2 and 3.28 cm^2, respectively, for the reference and the corrugated membrane). In Fig. 2b and e, it is possible to see a cross-section of the membranes that highlight the differences between the two designs. In the first case, the considered active region (between the ribs) is flat, while in the latter the membrane is corrugated in order to increase its effective area. The black colour of the printed parts (Fig. 2c and f) is due to the addition of the black pigment necessary to tune the curing depth of the resin with the laser of the SLA machine, already mentioned in the experimental section.

The tailoring of the debinding/sintering treatment was based on the results of DSC/TGA performed on the printed material (Fig. S1†). These analyses highlighted two exothermic peaks at 212 °C and 375 °C corresponding to the burning of the organic components in the cured part, concordant with the loss of mass detected by TGA. From DSC, the glass transition temperature T_g and the crystallization peak temperatures T_c of the glassy LAGP were also detected, respectively, at 497 °C and 623 °C. Based on these results, the debinding/sintering thermal treatment was chosen to be 0.2 °C min^{-1} up to 400 °C for 2 h (debinding), plus a second ramp at 5 °C min^{-1} up to 750 °C for 12 h (sinter-crystallization). The debinding step was carried out at a very low heating rate to limit the possible deformations of the structure and to allow the produced gases to be gradually evacuated from the samples.

Pictures of the 3D printed samples after this thermal treatment, which was identical for both planar and corrugated designs, are presented in Fig. 3a and b. All the parts maintained their original shape after sintering, without significant deformation or bending. From the cross-section SEM pictures, the shape difference between the two types of membranes is clearly visible (Fig. 3). Fig. 3c–f show the corrugation introduced in the LAGP membrane coming from the design implemented by SLA, in comparison with the reference flat membrane. Both membranes present a homogeneous and similar thickness of *ca.* 200 μm.

Fig. 4 shows the SEM microstructural characterization carried out at higher magnification on LAGP pellets (conventionally manufactured) and printed parts. Printed and sintered LAGP

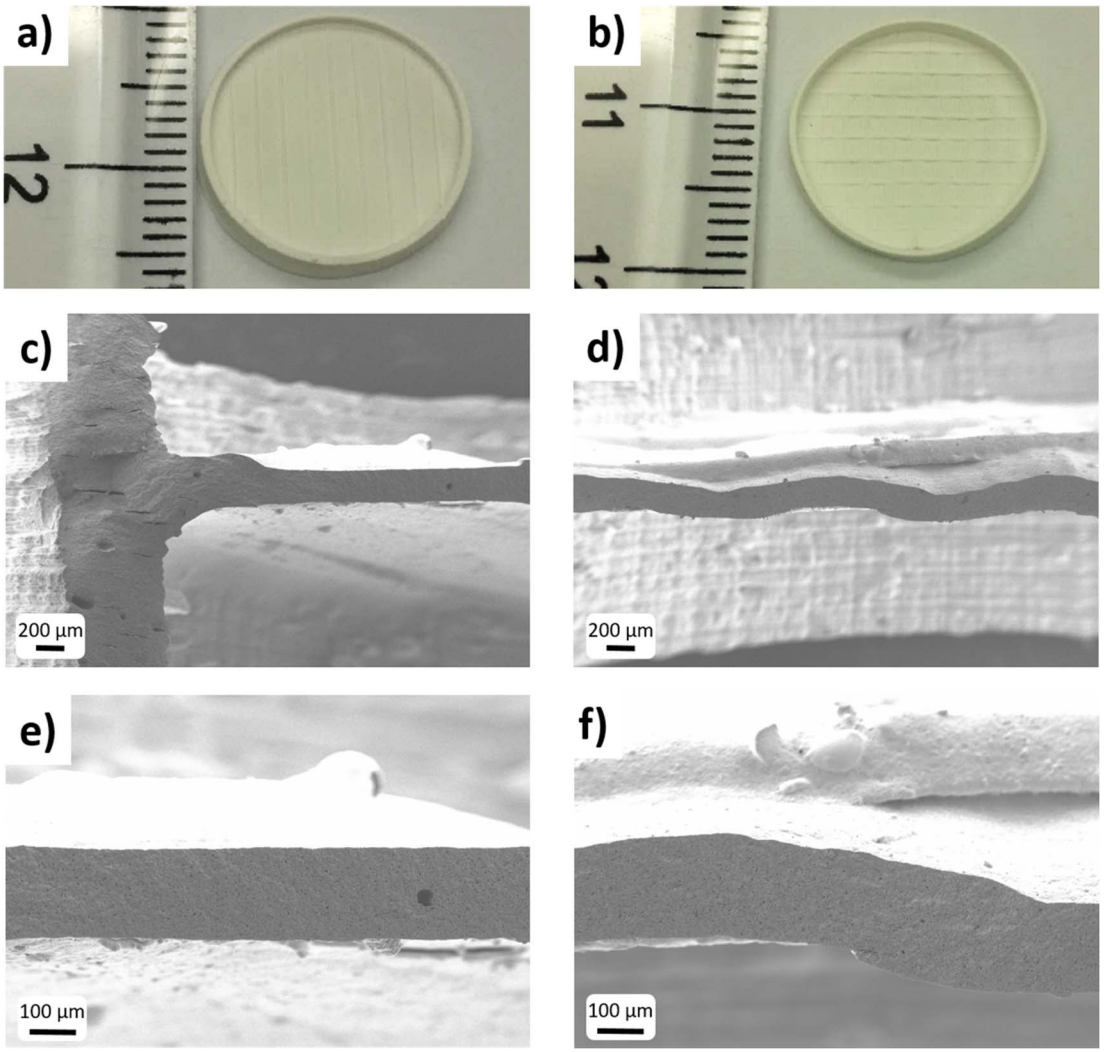

Fig. 3 Photos of the 3D printed LAGP membranes after the debinding/sintering treatment together with their SEM micrographs for both the considered shapes: reference (a, c and e) and corrugated (b, d and f).

shows slightly lower density in the SEM image (higher porosity). The relative density calculated based on the SEM images (through image analysis software) were found to be ≈90% and ≈85% for the pellet and the 3D printed part, respectively. The lower densification of the printed parts is likely due to a limited ceramic loading of the printable slurry. Up to now, it was not possible to increase the ceramic content of the paste to more than 65 wt%. Further addition of ceramic to the paste led to a dramatic increase in the viscosity compromising its printability. However, further work on increasing this value is ongoing. Importantly, no evidence of heterogeneities, secondary phases, or decomposition products was observed by SEM.

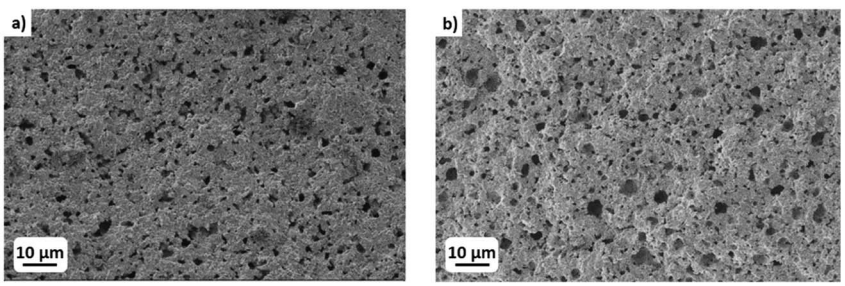

Fig. 4 SEM micrographs showing the microstructure and porosity of LAGP produced in the form of a pellet by a conventional manufacturing technique (a) and by SLA (b) after the debinding/sintering treatment (the pictures were collected on fractured surfaces).

For comparison purposes, XRD analyses of pellets and 3D printed parts after identical sintering treatments were also carried out (Fig. 5). XRD diffractograms show the same pattern for both LAGP samples after the sinter-crystallization thermal treatments. It is worth noting that LAGP is prone to form $AlPO_4$ and GeO_2 when exposed to long thermal treatments at temperatures higher than 750 °C in air, due to Li losses.[43] The formation of these phases is commonly correlated with an increase in the porosity in the material and to a decrease in the ionic conductivity due to both the lower density and the insulating nature of the formed $AlPO_4$. In the present case, no peaks related to $AlPO_4$ or GeO_2 phases were detected either in the pellets or in the 3D printed pieces, thus excluding any possible detrimental interaction due to the presence of the organic vehicle in the green state.

The electrochemical performances of 3D printed LAGP electrolytes were assessed through electrochemical impedance spectroscopy (EIS) on both printed geometries: the reference-planar and the corrugated membranes (Nyquist plots can be found in Fig. 6a). The measurements were conducted in a symmetrical configuration using sputtered gold as an electrode, Au/LAGP/Au. Area specific resistance (ASR) associated with the LAGP electrolyte was calculated as $ASR = R \times A$, where R is the resistance of the electrolyte (in Ω) and A is the area (in cm^2). In this calculation, with the aim of showing the improvement of the corrugation, the area of the membranes considered was the projected area, which is the same in both the reference-planar and corrugated samples. The resistance employed for the calculation was obtained after fitting the EIS spectra using the equivalent circuit described in the inset sketch of Fig. 6a (more details on the physical meaning of each element of the circuit are given in the ESI† in the section "EIS at different temperatures"). From the fitting, it was possible to calculate the *ASR* of each membrane, where the total resistance is considered as the sum of the contribution due to the grain boundaries and the bulk ($R_{TOT} = R_{gb} + R_b$). The values obtained are 311 Ω cm^2 and 267 Ω cm^2 for the reference and the corrugated membranes, respectively. These values clearly indicate that corrugated structures reduce the total ASR by 15%, which can be directly associated with the additional 15% area in the corrugated membrane. This demonstrates the potential effectiveness of 3D printing for increasing the performance by design, thus allowing superior power densities in all-solid-state batteries.

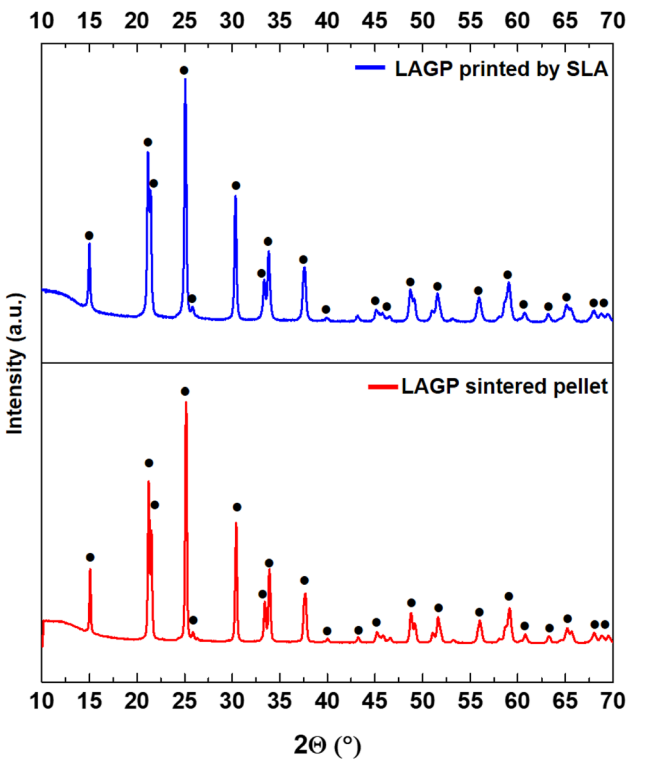

Fig. 5 XRD of LAGP produced in the form of a pellet and by SLA after the debinding/sintering treatment. The crystalline phase (•) was identified with the pattern of $LiGe_2(PO_4)_2$ (PDF #1-080-1924).

EIS measurements were also carried out between 25 °C and 75 °C on 3D printed LAGP (on both the reference membrane and the corrugated one) and on LAGP obtained as a pellet; the results are reported in the ESI† (Fig. S2, S3, and S4) and compared with values recorded in the literature for the same material. An Arrhenius-like behaviour was observed for all the samples indicating the thermally activated nature of the conduction phenomena taking place (Fig. 6b). Lower ASR values for corrugated LAGP membranes were also confirmed at higher temperatures. The activation energy measured on 3D printed LAGP was estimated to be 0.44 ± 0.02 eV, which is in good agreement with values reported in the literature for this material (0.41 ± 0.02 eV), indicating complete crystallization of the amorphous powder during the sintering process.[43]

Regarding the total ionic conductivity of printed LAGP, values of $\sigma = 6.4\ 10^{-5}$ S cm^{-1} at 25 °C were obtained (Fig. S4†). This conductivity is about half the value measured for pelletized LAGP samples yielding $\sigma = 2.6\ 10^{-4}$ S cm^{-1}, which is in good agreement with conductivities reported in the literature.[36,39,43] This discrepancy can be partially ascribed to a lower densification of the SLA printed material (Fig. 3), which, according to previous studies, could involve an exponential decay of the conductivity with increasing porosity.[44,45] Detailed analysis of the EIS data for printed parts yielded bulk conductivity values as high as $\sigma = 2.1\ 10^{-4}$ S cm^{-1} (Fig. S5†), which confirms good crystallization of the material and indicates a strong contribution of the grain boundary to the total resistance. The use of sintering aids as additives in the formulation of the glass or of the ceramic paste will be explored in the future to achieve higher densification values.

In order to provide stable interfaces against metallic Li, a thin metallic Ge layer was deposited on both sides of the LAGP electrolytes, following the strategy reported by Liu *et al.*[46] According to their work, a Ge protective layer suppresses the Ge^{4+} reduction and promotes contact with Li metal. In the present work, the Ge protective layer was deposited by thermal evaporation, reaching a thickness of 200 nm on both sides of the 3D-printed solid electrolytes before placing them in contact with metallic Li. EIS was performed on symmetric cells with Li electrodes, considering both planar and corrugated geometry. Fig. 7a shows the results obtained, along with the

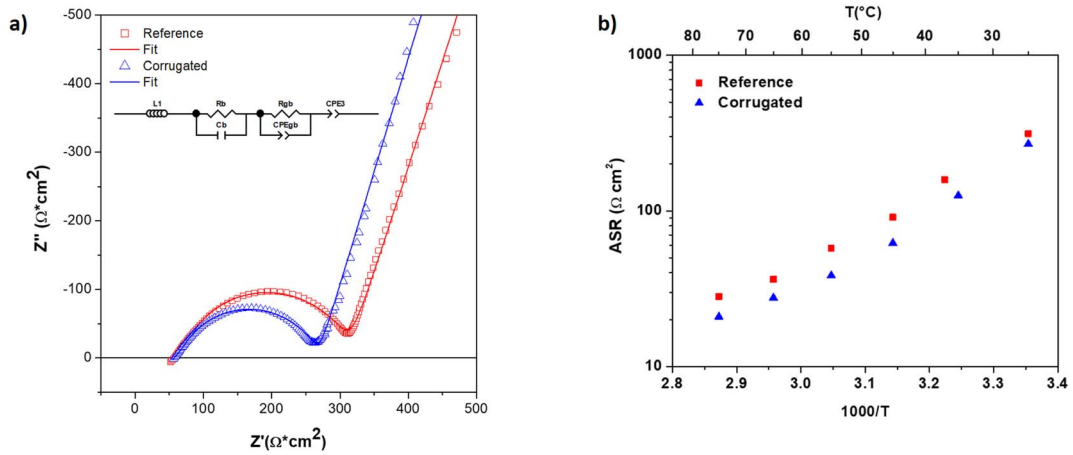

Fig. 6 Electrochemical impedance spectroscopy measured on reference and corrugated LAGP membranes produced *via* SLA coated with Au (a); ASR values recorded at different temperatures for both reference and corrugated membranes of LAGP produced *via* SLA and coated with Au (b).

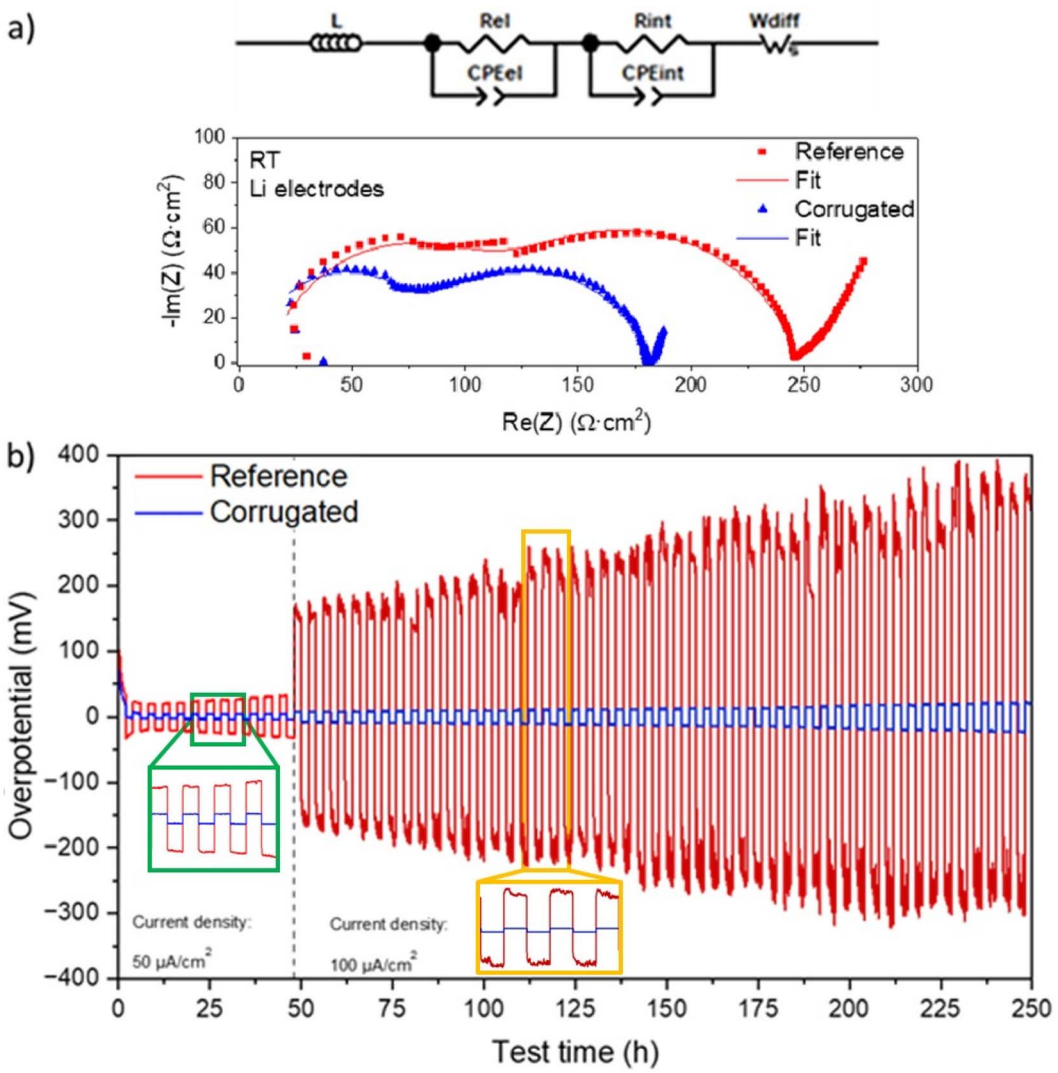

Fig. 7 Electrochemical impedance spectroscopy spectra of Li symmetrical cells assembled on reference and corrugated printed electrolytes and the relative equivalent circuit (a). Galvanostatic cycling of the printed electrolytes in a Li|Ge-LAGP-Ge|Li configuration (b).

corresponding equivalent circuit used for the fitting. From this analysis, it is possible to appreciate the resistance of the two cells, proving values comparable to those of symmetric cells with Au ion-blocking electrodes (discussed before in this section) and low enough to enable cycling in a solid-state battery. The estimated ionic conductivities found for the symmetric Li cells are well in agreement with the previous measurements (*c.a.* 10^{-4} S cm^{-1}). The reduction of the electrolyte resistance (correlated with the first semicircle in the Nyquist plot) is comparable with the expected improvement due to the increase in the active area by corrugation ($\approx$15%). Further improvement of around 25% can be ascribed to the Li|LAGP interface, indicating a better contact between the electrode and the electrolyte in the case of corrugated membranes.

The same samples were subsequently subjected to plating–stripping cycles in galvanostatic mode for over 250 hours at two different current densities to evaluate the stability of the LAGP|Li interface in *operando* conditions. After an initial stabilization time lasting a couple of cycles, the trend of the overpotential shows the typical profile for stripping/plating tests. The reference-planar membrane shows an initial overpotential of 20 mV, increased up to 30 mV in the first 48 hours of the test at 50 μA cm^{-2}. On the other hand, the cell based on a corrugated electrolyte shows a stable overpotential of 5 mV over the first 48 hours of the test. At a higher current density (100 μA cm^{-2}), the overpotential of both cells increased over time. In the case of the reference cell, the initial value was 160 mV, reaching up to 325 mV at the end of the test. Noticeably, the corrugated one revealed much lower overpotential values of 8 mV and 22 mV at the beginning and at the end of the test, respectively.

These results clearly show that the deposition of Ge as a protective layer against Li is a very effective strategy to block the reactivity between Li and LAGP, which typically results in a rapid increase of the overpotential (>2 V) after the first cycles.[46] In addition, and more interestingly, corrugated surfaces not only reduce the resistance of the cell due to a straightforward increase of the active area but also lower the contact resistance between the electrolyte and the electrode, which results in outstandingly small overpotentials and remarkably high stability over time.[41,43] Since this enhancement is only observed for corrugated electrolytes (and not for their flat counterparts), one can associate it with the additional 3D structuration present in the corrugated samples (*cf.* Fig. 2a and d). This three-dimensional microstructure is expected to increase the surface area, lowering the local current density while acting as a host matrix for lithium nucleation during plating/stripping cycles and therefore, better accommodating volume changes and offering lower interfacial resistances. Further work is ongoing to fine-tune 3D printed microstructures for anode-less approaches.

Overall, 3D printed self-supported LAGP electrolytes were shown here as promising solid-state electrolytes for ASSB applications with potential for improvement of electrolyte and electrolyte-lithium resistances by design.

4 Conclusions

In the present work, 3D printing was successfully employed to produce $Li_{1.5}Al_{0.5}Ge_{1.5}P_3O_{12}$ solid electrolytes for all-solid-state lithium-metal batteries. To the best of the authors' knowledge, this represents the first example of direct 3D printing of LAGP and the first application of stereolithography for ceramic battery manufacturing of electrolytes. Furthermore, this work explored the possibility of increasing the active area of battery cells while maintaining the same overall dimensions by employing corrugated electrolytes. Such corrugated electrolytes were successfully fabricated by SLA, resulting in a reduction of *ca.* 15% in their total area specific resistance, in comparison with their flat printed counterparts. Despite the marginal increase in the effective area, this study represents a proof of concept that opens the door to future development of more complex geometries with higher aspect ratios which will further improve the performance of next generation batteries.

Thermally evaporated Ge protective layers were deposited on printed LAGP electrolytes providing the necessary stability *vs.* Li for carrying out galvanostatic cycling on Li/Ge-LAGP-Ge/Li symmetrical cells. EIS measurements on such symmetrical cells showed that beyond the straightforward enhancement due to an increase in the active area, corrugated electrolytes showed an additional 25% reduction of the total resistance which is unambiguously ascribed to an improved electrolyte/Li-metal interface. Moreover, cycling tests of corrugated samples showed a remarkably low overpotential with a small increase over 250 hours of operation under standard conditions (0.1 mA cm^{-2} and 2 hour cycle). Although the origin of the better performance and stability of corrugated samples is still under investigation, additional three-dimensional microstructures present in corrugated electrolytes are likely the cause for this. Such 3D-printed microstructures notably increase the interfacial area while probably acting as lithium hosts for more homogeneous and continuous nucleation during plating/stripping cycles. In any case, the observed enhancement anticipates a powerful approach based on engineering interfaces by 3D printing for application in anode-less strategies.

Overall, the present work shows the promising role of 3D printing technologies in delivering a new generation of all-solid-state batteries with superior volumetric energy density and enhanced stability by design.

5 Author contributions

Conceptualization: AGS, MT, AM, and AT; investigation: AGS, MNE, SA, CDS, and AP; formal analysis: AGS, JCGR, AP, GA, and PLA; funding acquisition: AGS, MT, MCC, and AT; supervision: MCC, PLA, and AT; writing – original draft: AGS; writing – review editing: AGS, JCGR, AP, MT, GA, MCC, PLA, AM, and AT.

Conflicts of interest

There are no conflicts of interest.

Acknowledgements

The authors want to acknowledge the financial support of the Spanish Ministry of Science and Innovation (PID2019-107106RB-C31, 3DPASSION; PID2019-107106RB-C33, and 3DACCESS) and Generalitat de Catalunya (2021 SGR 00750). This project has received funding from the European Union's Horizon 2020 research and innovation program under the Marie Skłodowska-Curie grant agreement No. 841937 (project 3D-PRESS). J. C. G.-R. acknowledges the financial support provided by the European Union's Horizon 2020 research and innovation program under the Marie Skłodowska-Curie Grant Agreement No. 801342 (Tecniospring INDUSTRY), as well as by the Agency for Business Competitiveness of the Government of Catalonia.

Notes and references

1 A. Armand and J.-M. Tarascon, Building better batteries, *Nature*, 2008, **451**, 652–657.

2 X. Q. Zhang, C. Z. Zhao, J. Q. Huang and Q. Zhang, Recent Advances in Energy Chemical Engineering of Next-Generation Lithium Batteries, *Engineering*, 2018, **4**, 831–847, DOI: **10.1016/j.eng.2018.10.008**.

3 Y. Jie, X. Ren, R. Cao, W. Cai and S. Jiao, Advanced Liquid Electrolytes for Rechargeable Li Metal Batteries, *Adv. Funct. Mater.*, 2020, **30**, 1–23, DOI: **10.1002/adfm.201910777**.

4 S. Chen, K. Wen, J. Fan, Y. Bando and D. Golberg, Progress and future prospects of high-voltage and high-safety electrolytes in advanced lithium batteries: From liquid to solid electrolytes, *J. Mater. Chem. A*, 2018, **6**, 11631–11663, DOI: **10.1039/c8ta03358g**.

5 Y. Chen, K. Wen, T. Chen, X. Zhang, M. Armand and S. Chen, Recent progress in all-solid-state lithium batteries: The emerging strategies for advanced electrolytes and their interfaces, *Energy Storage Mater.*, 2020, **31**, 401–433, DOI: **10.1016/j.ensm.2020.05.019**.

6 Q. Zhao, S. Stalin, C. Z. Zhao and L. A. Archer, Designing solid-state electrolytes for safe, energy-dense batteries, *Nat. Rev. Mater.*, 2020, **5**, 229–252, DOI: **10.1038/s41578-019-0165-5**.

7 S. Tang, W. Guo and Y. Fu, Advances in Composite Polymer Electrolytes for Lithium Batteries and Beyond, *Adv. Energy Mater.*, 2021, **11**, 1–29, DOI: **10.1002/aenm.202000802**.

8 X. Yu and A. Manthiram, A review of composite polymer-ceramic electrolytes for lithium batteries, *Energy Storage Mater.*, 2021, **34**, 282–300, DOI: **10.1016/j.ensm.2020.10.006**.

9 M. Zhang, H. Mei, P. Chang and L. Cheng, 3D printing of structured electrodes for rechargeable batteries, *J. Mater. Chem. A*, 2020, **8**, 10670–10694, DOI: **10.1039/d0ta02099k**.

10 J. Wang, Q. Sun, X. Gao, C. Wang, W. Li, F. B. Holness, M. Zheng, R. Li, A. D. Price, X. Sun, T. K. Sham and X. Sun, Toward High Areal Energy and Power Density Electrode for Li-Ion Batteries via Optimized 3D Printing Approach, *ACS Appl. Mater. Interfaces*, 2018, **10**, 39794–39801, DOI: **10.1021/acsami.8b14797**.

11 S. Zhou, I. Usman, Y. Wang and A. Pan, 3D printing for rechargeable lithium metal batteries, *Energy Storage Mater.*, 2021, **38**, 141–156, DOI: **10.1016/j.ensm.2021.02.041**.

12 Z. Lyu, G. J. H. Lim, J. J. Koh, Y. Li, Y. Ma, J. Ding, J. Wang, Z. Hu, J. Wang, W. Chen and Y. Chen, Design and Manufacture of 3D-Printed Batteries, *Joule*, 2021, **5**, 89–114, DOI: **10.1016/j.joule.2020.11.010**.

13 J. C. Ruiz-Morales, A. Tarancón, J. Canales-Vázquez, J. Méndez-Ramos, L. Hernández-Afonso, P. Acosta-Mora, J. R. Marín Rueda and R. Fernández-González, Three dimensional printing of components and functional devices for energy and environmental applications, *Energy Environ. Sci.*, 2017, **10**, 846–859, DOI: **10.1039/c6ee03526d**.

14 A. Tarancón, V. Esposito, M. Torrell, M. Di Vece, J. S. Son, P. Norby, S. Barg, P. S. Grant, A. Vogelpoth, S. Linnenbrink, M. Brucki and T. Scopphoven, 2022 roadmap on 3D printing for energy Journal of Physics: Energy OPEN ACCESS, *J. Phys.: Energy*, 2022, **4**, 011501.

15 A. Tarancón and V. Esposito, *3D Printing for Energy Applications*, 2021.

16 S. Anelli, M. Rosa, F. Baiutti, M. Torrell, V. Esposito and A. Tarancón, Hybrid-3D printing of symmetric solid oxide cells by inkjet printing and robocasting, *Addit. Manuf.*, 2022, **51**, 102636.

17 E. Peng, D. Zhang and J. Ding, Ceramic Robocasting: Recent Achievements, Potential, and Future Developments, *Adv. Mater.*, 2018, **30**, 1–14, DOI: **10.1002/adma.201802404**.

18 S. Zakeri, M. Vippola and E. Levänen, A comprehensive review of the photopolymerization of ceramic resins used in stereolithography, *Addit. Manuf.*, 2020, **35**, 101177, DOI: **10.1016/j.addma.2020.101177**.

19 A. Zocca, P. Colombo, C. M. Gomes and J. Günster, Additive Manufacturing of Ceramics: Issues, Potentialities, and Opportunities, *J. Am. Ceram. Soc.*, 2015, **98**, 1983–2001, DOI: **10.1111/jace.13700**.

20 N. Guo and M. C. Leu, Additive manufacturing: Technology, applications and research needs, *Front. Mech. Eng.*, 2013, **8**, 215–243, DOI: **10.1007/s11465-013-0248-8**.

21 A. Pesce, A. Hornés, M. Núñez, A. Morata, M. Torrell and A. Tarancón, 3D printing the next generation of enhanced solid oxide fuel and electrolysis cells, *J. Mater. Chem. A*, 2020, **8**, 16926–16932, DOI: **10.1039/d0ta02803g**.

22 S. Masciandaro, M. Torrell, P. Leone and A. Tarancón, Three-dimensional printed yttria-stabilized zirconia self-supported electrolytes for solid oxide fuel cell applications, *J. Eur. Ceram. Soc.*, 2019, **39**, 9–16, DOI: **10.1016/j.jeurceramsoc.2017.11.033**.

23 K. H. Choi, D. B. Ahn and S. Y. Lee, Current Status and Challenges in Printed Batteries: Toward Form Factor-Free, Monolithic Integrated Power Sources, *ACS Energy Lett.*, 2018, **3**, 220–236, DOI: **10.1021/acsenergylett.7b01086**.

24 Y. Gu, A. Wu, H. Sohn, C. Nicoletti, Z. Iqbal and J. F. Federici, Fabrication of rechargeable lithium ion batteries using water-based inkjet printed cathodes, *J. Manuf. Process*, 2015, **20**, 198–205, DOI: **10.1016/j.jmapro.2015.08.003**.

25 A. Kushwaha, M. K. Jangid, B. B. Bhatt, A. Mukhopadhyay and D. Gupta, Inkjet-Printed Environmentally Friendly

Graphene Film for Application as a High-Performance Anode in Li-Ion Batteries, *ACS Appl. Energy Mater.*, 2021, **4**, 7911–7921, DOI: 10.1021/acsaem.1c01249.

26 T. S. Wei, B. Y. Ahn, J. Grotto and J. A. Lewis, 3D Printing of Customized Li-Ion Batteries with Thick Electrodes, *Adv. Mater.*, 2018, **30**, 1–7, DOI: 10.1002/adma.201703027.

27 C. Liu, X. Cheng, B. Li, Z. Chen, S. Mi and C. Lao, Fabrication and characterization of 3D-printed highly-porous 3D LiFePO4 electrodes by low temperature direct writing process, *Mater.*, 2017, **10**, DOI: 10.3390/ma10080934.

28 J. Li, X. Liang, F. Liou and J. Park, Macro-/Micro-Controlled 3D Lithium-Ion Batteries via Additive Manufacturing and Electric Field Processing, *Sci. Rep.*, 2018, **8**, 1–12, DOI: 10.1038/s41598-018-20329-w.

29 K. Sun, T. S. Wei, B. Y. Ahn, J. Y. Seo, S. J. Dillon and J. A. Lewis, 3D printing of interdigitated Li-ion microbattery architectures, *Adv. Mater.*, 2013, **25**, 4539–4543, DOI: 10.1002/adma.201301036.

30 S. Zekoll, C. Marriner-Edwards, A. K. O. Hekselman, J. Kasemchainan, C. Kuss, D. E. J. Armstrong, D. Cai, R. J. Wallace, F. H. Richter, J. H. J. Thijssen and P. G. Bruce, Hybrid electrolytes with 3D bicontinuous ordered ceramic and polymer microchannels for all-solid-state batteries, *Energy Environ. Sci.*, 2018, **11**, 185–201, DOI: 10.1039/c7ee02723k.

31 Y. He, S. Chen, L. Nie, Z. Sun, X. Wu and W. Liu, Stereolithography Three-Dimensional Printing Solid Polymer Electrolytes for All-Solid-State Lithium Metal Batteries, *Nano Lett.*, 2020, **20**, 7136–7143, DOI: 10.1021/acs.nanolett.0c02457.

32 M. Cheng, Y. Jiang, W. Yao, Y. Yuan, R. Deivanayagam, T. Foroozan, Z. Huang, B. Song, R. Rojaee, T. Shokuhfar, Y. Pan, J. Lu and R. Shahbazian-Yassar, Elevated-Temperature 3D Printing of Hybrid Solid-State Electrolyte for Li-Ion Batteries, *Adv. Mater.*, 2018, **30**, 1–10, DOI: 10.1002/adma.201800615.

33 K. Fu, Y. Wang, C. Yan, Y. Yao, Y. Chen, J. Dai, S. Lacey, Y. Wang, J. Wan, T. Li, Z. Wang, Y. Xu and L. Hu, Graphene Oxide-Based Electrode Inks for 3D-Printed Lithium-Ion Batteries, *Adv. Mater.*, 2016, **28**, 2587–2594, DOI: 10.1002/adma.201505391.

34 D. W. McOwen, S. Xu, Y. Gong, Y. Wen, G. L. Godbey, J. E. Gritton, T. R. Hamann, J. Dai, G. T. Hitz, L. Hu and E. D. Wachsman, 3D-Printing Electrolytes for Solid-State Batteries, *Adv. Mater.*, 2018, **30**, 1–7, DOI: 10.1002/adma.201707132.

35 Y. Zhu, X. He and Y. Mo, Origin of Outstanding Stability in the Lithium Solid Electrolyte Materials: Insights from Thermodynamic Analyses Based on First-Principles Calculations, *ACS Appl. Mater. Interfaces*, 2015, **7**, 23685–23693, DOI: 10.1021/acsami.5b07517.

36 M. Hou, F. Liang, K. Chen, Y. Dai and D. Xue, Challenges and perspectives of {NASICON}-type solid electrolytes for all-solid-state lithium batteries, *Nanotechnology*, 2020, **31**, 132003, DOI: 10.1088/1361-6528/ab5be7.

37 Z. Wu, Z. Xie, A. Yoshida, Z. Wang, X. Hao, A. Abudula and G. Guan, Utmost limits of various solid electrolytes in all-solid-state lithium batteries: A critical review, *Renewable Sustainable Energy Rev.*, 2019, **109**, 367–385, DOI: 10.1016/j.rser.2019.04.035.

38 A. Rossbach, F. Tietz and S. Grieshammer, Structural and transport properties of lithium-conducting NASICON materials, *J. Power Sources*, 2018, **391**, 1–9, DOI: 10.1016/j.jpowsour.2018.04.059.

39 R. DeWees and H. Wang, Synthesis and Properties of NaSICON-type LATP and LAGP Solid Electrolytes, *ChemSusChem*, 2019, **12**, 3713–3725, DOI: 10.1002/cssc.201900725.

40 H. Kun, W. Yanhang, Z. Chengkui, Z. Huifeng, L. Yonghua, C. Jiang, H. Bin and M. Juanrong, Influence of Al_2O_3 additions on crystallization mechanism and conductivity of $Li_2OGe_2OP_2O_5$ glass-ceramics, *Phys. B*, 2011, **406**, 3947–3950, DOI: 10.1016/j.physb.2011.07.033.

41 Y. Zhu, Y. Zhang and L. Lu, Influence of crystallization temperature on ionic conductivity of lithium aluminum germanium phosphate glass-ceramic, *J. Power Sources*, 2015, **290**, 123–129, DOI: 10.1016/j.jpowsour.2015.04.170.

42 Z. Liu, S. Venkatachalam and L. Van Wüllen, Structure, phase separation and Li dynamics in sol-gel-derived Li1 + xAl_xGe_2 – $X(PO_4)_3$, *Solid State Ionics*, 2015, **276**, 47–55, DOI: 10.1016/j.ssi.2015.03.018.

43 C. R. Mariappan, C. Yada, F. Rosciano and B. Roling, Correlation between micro-structural properties and ionic conductivity of $Li_{1.5}Al_{0.5}Ge_{1.5}(PO_4)_3$ ceramics, *J. Power Sources*, 2011, **196**, 6456–6464, DOI: 10.1016/j.jpowsour.2011.03.065.

44 M. B. Dixit, M. Regala, F. Shen, X. Xiao and K. B. Hatzell, Tortuosity Effects in Garnet-Type Li 7 La 3 Zr 2 O 12 Solid Electrolytes, *ACS Appl. Mater. Interfaces*, 2019, **11**, 2022–2030, DOI: 10.1021/acsami.8b16536.

45 Z. hao GUO, X. hai LI, Z. xing WANG, H. jun GUO, W. jie PENG, Q. yang HU, G. chun YAN and J. xi WANG, Empirical decay relationship between ionic conductivity and porosity of garnet type inorganic solid-state electrolytes, *Trans. Nonferrous Met. Soc. China*, 2022, **32**, 3362–3373, DOI: 10.1016/S1003-6326(22)66025-4.

46 Y. Liu, C. Li, B. Li, H. Song, Z. Cheng, M. Chen, P. He and H. Zhou, Germanium Thin Film Protected Lithium Aluminum Germanium Phosphate for Solid-State Li Batteries, *Adv. Energy Mater.*, 2018, **8**, 1–7, DOI: 10.1002/aenm.201702374.

